Influence of Nickel Loading on Reduced Graphene Oxide-Based Nickel Catalysts for the Hydrogenation of Carbon Dioxide to Methane

Nur Diyan Mohd Ridzuan [1], **Maizatul Shima Shaharun** [1,*], **Kah Mun Lee** [1], **Israf Ud Din** [2] **and Poppy Puspitasari** [3]

1   Fundamental and Applied Sciences Department, Universiti Teknologi PETRONAS, 32610 Seri Iskandar, Perak, Malaysia; nur_17007454@utp.edu.my (N.D.M.R.); kahmunlee19@gmail.com (K.M.L.)
2   Department of Chemistry, College of Science and Humanities, Prince Sattam bin Abdulaziz University, 16278 Al-kharj, Saudi Arabia; drisraf@yahoo.com
3   Mechanical Engineering Department, Engineering Faculty, State University of Malang, 5 Semarang Str., 65145 Malang, East Java, Indonesia; poppy@um.ac.id
*   Correspondence: maizats@utp.edu.my

Abstract: In this study, a series of novel nickel catalysts supported on reduced graphene oxide nanosheets (Ni/rGO) with Ni loadings of 10, 15 and 20 wt% were successfully synthesized via the incipient wetness impregnation method. The physicochemical properties of the catalysts and rGO support were thoroughly characterized by thermogravimetric analyser, X-ray diffraction, fourier-transform infrared spectroscopy, Raman spectroscopy, N_2 adsorption-desorption, temperature programmed reduction, temperature programmed CO_2 desorption and field emission scanning electron microscopy with energy dispersive X-ray spectroscopy. The properties of the catalysts are correlated to its catalytic activity for CO_2 methanation which were investigated using three-phase slurry reactor at low temperature and pressure of 240 °C and 10 bar, respectively. Among the three catalysts of different Ni loading, Ni_{15}/rGO shows the highest activity of 51% conversion of CO_2 with total selectivity towards CH_4. N_2-physisorption and CO_2-TPD analysis suggest that high catalytic performance of Ni_{15}/rGO is attributed to the high surface area, strong basic sites and special support effect of rGO in anchoring the active metal.

Keywords: methanation; carbon dioxide; nickel-based catalyst; graphene support

1. Introduction

The concentration of carbon dioxide (CO_2), a major component of greenhouse gases, is rapidly increasing in the atmosphere [1]. With over 30 gigaton (Gt) emissions a year, high atmospheric CO_2 is alarming as it will create critical risks for the Earth's climate system [2]. Due to the global concern about the climate change, CO_2 conversion into valuable low-carbon fuels such as methane (CH_4) is seen as a viable solution to reduce anthropogenic CO_2 emissions [3]. CO_2 methanation, as in Equation (1), was initially reported by Sabatier and Senderens in 1902 [4]. Ideally in a power-to-gas (P2G) technology, CH_4 will be produced from Sabatier reaction by reacting CO_2 recovered from industrial process with hydrogen (H_2) from water splitting.

$$CO_2 + 4H_2 \rightarrow CH_4 + 2H_2O; \Delta H_{298K} = -164.4 \text{ kJ/mol} \tag{1}$$
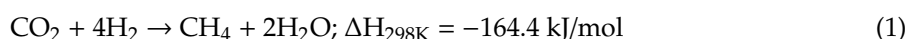
An active catalyst is needed to achieve acceptable selectivity and conversion for CO_2 methanation in which transition metals from group VII have been commonly employed. Even though studies

suggested that ruthenium is the most active metal for CO_2 methanation [5,6], nickel-based catalysts are more commonly employed in industry owing to their high performance to cost ratio, feasibility and easy availability [7]. However, under the severe reaction conditions, Ni catalysts may be deactivated due to the sintering of Ni particles, formation of mobile nickel sub-carbonyls and formation of carbon deposits [8,9]. In order to improve their activity, Ni catalysts are supported on various oxides such as Al_2O_3 [10–12], SiO_2 [13], ZrO_2 [14,15] and CeO_2 [16]. This strategy can enhance dispersion, avoid agglomeration of Ni, resist sintering of carbon, and increase exposed active sites [13,17].

Following its first isolation in 2004 by Novoselov and Geim [18], graphene has sparked significant attention both for fundamental aspects and application studies [19]. Graphene is a sp^2- hybridized carbon-based material with a hexagonal monolayer network forming a two dimensional structure [20]. High surface area, thermostability and uniform porosity are among the interesting features of graphene. These properties make it ideal to be used in heterogeneous catalysis either as a catalyst or support [21]. Even though it is seen as a promising material, studies that use graphene as a catalyst support in the heterogeneous catalysis field are still limited [21].

The highly exothermic process of CO_2 methanation requires efficient heat removal to avoid backward reactions. Fixed-bed reactors are commonly reported for the methanation process due to their ease of design and lower cost of maintenance and operation. However, the high heat produced from the reaction can accumulate and cause severe hot spot in catalysts, leading to their deactivation [22]. Hence, the focus has shifted towards the use of three-phase slurry reactors since they offer good temperature control properties, nearly isothermal operation and good heat and mass transfer [23,24]. The presence of a liquid phase in the reactor will contribute also to a better removal of the heat from the exothermic CO_2 methanation reaction.

Herein, Ni/rGO catalysts were synthesized via an incipient wetness impregnation method using a commercial reduced graphene oxide nanosheet support (rGO) for application in CO_2 methanation. The commercial support and catalysts were thoroughly characterized beforehand using spectroscopic and microscopic methods. A CO_2 methanation study was carried out in a three-phase slurry reactor over Ni/rGO at different metal loadings in which the conversion is correlated with their characteristics. To the best of our knowledge, there are limited reported studies on the application of graphene as catalyst support for CO_2 methanation.

2. Results

2.1. Physicochemical Properties of rGO and Ni/rGO

A thermogram of the rGO support showing the DTG curve is shown in Figure 1. The TGA profile of rGO implies that rGO has excellent thermal stability because heating up to 900 °C only resulted in a 15.14% weight loss. The first weight loss step is observed between 100 °C to 150 °C which is caused by the loss of physisorbed water from the sample (2.28% loss). The presence of physisorbed water on the rGO surface is due to the porous characteristics and oxygen functional groups on the edge of graphene [20,25,26]. Further heating to the calcination temperature of 400 °C only resulted in another 4% degradation; hence, rGO does not degrade in the Ni/rGO synthesis step. High thermal stability of the rGO is important to avoid decomposition which could result in metal sintering during CO_2 methanation; hence, reducing the conversion efficiency. At elevated reaction temperatures, rGO can anchor the Ni active phase without being decomposed during CO_2 methanation reaction.
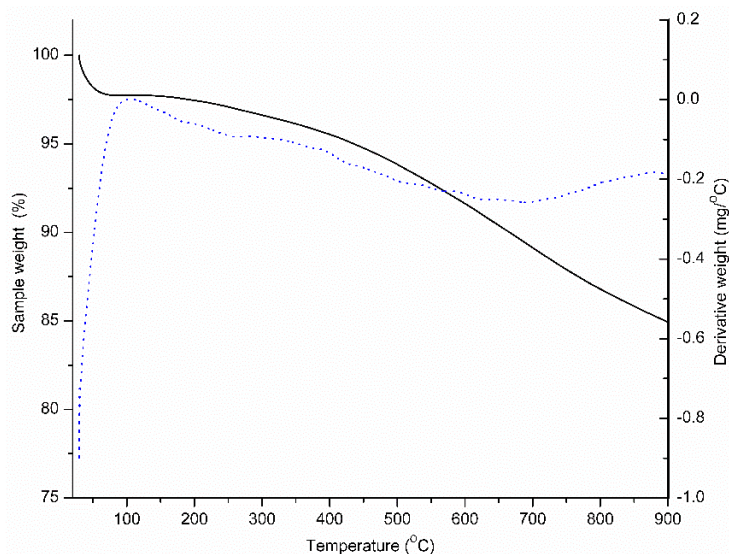
Figure 1. Thermogram of rGO.

From Raman spectrum in Figure 2, three fundamental vibrations are observed in the range of 1300 to 3000 cm^{-1}. D band, the breathing mode of κ-point phonons, is observed at 1352 cm^{-1} with relatively low intensity which indicates the presence of defects in rGO. Even though the presence of defects can disrupt the structure of carbon atoms at the graphitic edges [27,28] but it can also provide active sites for chemical reactions [29].
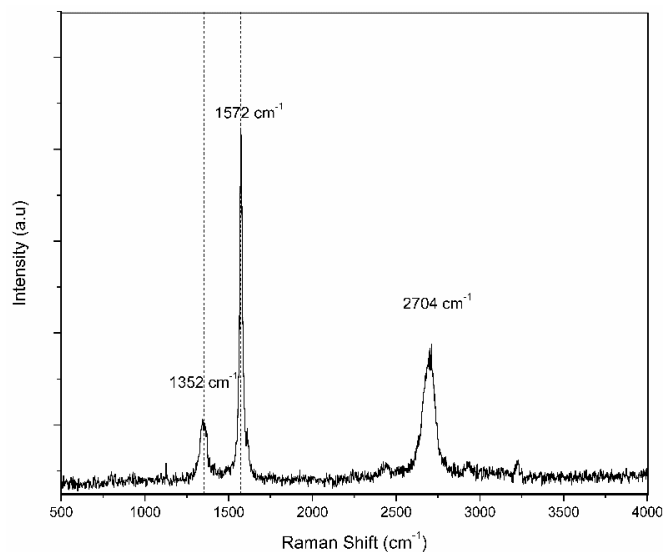

Figure 2. Raman spectrum of rGO.

The G vibration band, assigned to the E$_{2g}$ phonon of *sp*^{2} C atoms in graphite single crystals [30], appears at 1572 cm^{-1}. As compared to rGO synthesized according to the literature [26,31], this commercial rGO has a sharper G band which indicates a higher *sp*^{2} domain and lower degree of disorder [28]. The 2D band of rGO is observed at 2704 cm^{-1}. The I$_{2D}$/I$_G$ ratio can give insights on the graphene layers [27,32]. The result shows that I$_{2D}$/I$_G$ <1; hence, the rGO is multilayer. Upon impregnation of Ni onto rGO, the Raman spectrum is blue-shifted. The frequency shift of the Raman spectra of graphene was explained by Dervishi et al. who indicated that the increase in Raman shift of D and G bands indicates an increase in defects size [33]. Apart from that, the I$_D$/I$_G$ ratio was found to increase as the defect density increases. The intensity ratio of rGO and Ni$_{15}$/rGO is almost similar,

possibly suggesting the defect density does not increase due to Ni impregnation but only the defect size increases in the graphene layer.

Figure 3 depicts the X-ray diffractograms of rGO and Ni/rGO catalysts. XRD pattern of rGO support shows good agreement with the hexagonal phase of the graphene crystal lattice. A major peak at 26.52° is indexed to the (002) facet of graphite crystals [34]. This peak describes the layers of rGO that are stacked at an interlayer spacing (*d*) of 0.336 nm [35]. The calculated crystallite size (L_c) in the stacking direction and width (L_a) of each rGO layer are 12.27 nm and 25.37 nm, respectively. Therefore, there are about 36 graphitic layers in each rGO crystal. The sharp and intense peak reflects the high crystallinity of rGO due to the structure that is only edge-oxidized, so its stacking is more comparable to well-ordered graphite. XRD patterns of synthesized rGO from other studies show broader (002) peaks due to poor ordering of the sheets along the stacking direction [25,26,36]. Another peak at 43.80° is indexed to the (100) plane of rGO. The commercial rGO used in this study is a multiple layer carbon allotrope where each layer consists of carbon atoms arranged in a honeycomb fashion with defects and oxygen functional groups at the edge [31]. After Ni is impregnated onto rGO, the (002) peak of rGO is observed with same intensity and position as in pristine rGO. This observation suggests that there was no disruption of the rGO crystallinity. All Ni/rGO catalysts reflect NiO peaks that are consistent with those of cubic phase which shows the viability of the wetness impregnation method to support Ni onto rGO. Diffraction peaks at 37.07°, 43.27°, 62.72°, 75.16° and 79.13° are assigned to the (111), (200), (220), (311) and (222) lattice planes, respectively. The intensity of the NiO peaks increases with increasing Ni content from 10 to 20 wt.% due to the formation of larger NiO crystals on the rGO [37]. The crystallite size (D) of NiO on Ni_{10}/rGO, Ni_{15}/rGO and Ni_{20}/rGO catalysts are calculated from Scherrer equation at peak (111) and are shown in Table 1.
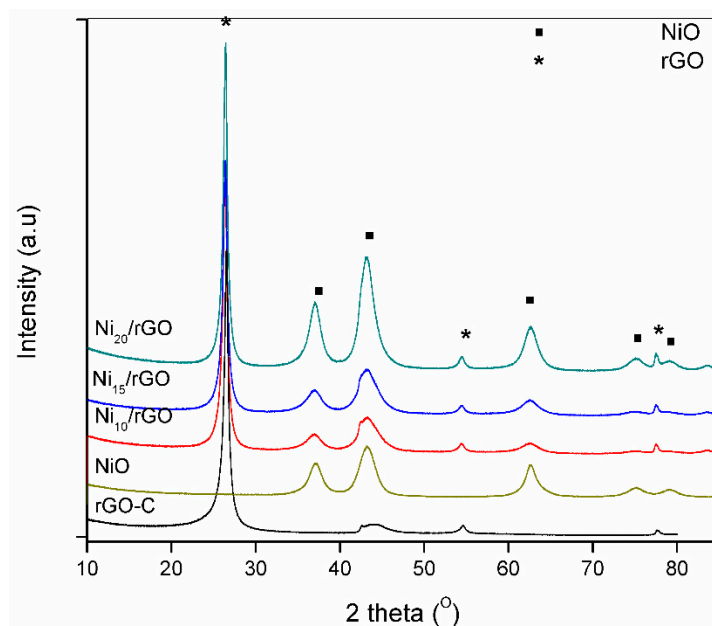

Figure 3. X-ray diffractogram of rGO support, NiO and Ni/rGO catalysts.

Table 1. Textural properties of, rGO, NiO and Ni/rGO with different Ni content.

Sample	S_{BET} (m^2/g)	Pore Volume (cm^3/g)	Pore Diameter (nm)	Ni Crystallite Size (nm)
rGO	258	0.39	7.09	-
NiO	177	0.25	4.14	5.48
Ni_{10}/rGO	126	0.35	10.2	4.49
Ni_{15}/rGO	140	0.31	8.08	4.58
Ni_{20}/rGO	122	0.32	9.16	5.36

Isotherms of rGO and Ni/rGO catalysts are presented in Figure 4, while comparative values obtained from surface area and porosity analysis are shown in Table 1. rGO exhibits a Type IV isotherm with H3 hysteresis loop based on the IUPAC classification [38]. rGO is a mesoporous material (its pores range from 2–50 nm) with aggregates of plate-like particles so the pores have a slit shape [13,39]. The BET surface area and BJH pore volume of rGO are 258 $m^2\,g^{-1}$ and 0.39 $cm^3\,g^{-1}$, respectively. A sharp increase at P/P_o is observed due to the presence of micropores (with pore sizes of less than 2 nm). rGO has a micropore surface area of 43 $m^2\,g^{-1}$ with a pore volume of 0.019 $cm^3\,g^{-1}$. The porous structure and high surface area features of rGO can serve as sites for Ni dispersion and active sites for chemical reactions. The isotherms and hysteresis loop patterns of the catalysts are like those of the rGO support. Furthermore, the pore volume of rGO decreases when Ni is loaded. Therefore, these results suggest that Ni nanoparticles are distributed and dispersed on the rGO surface and pores since the Ni crystallite size is smaller than the rGO pore diameter [40]. The amount of N_2 adsorbed decreased due to loading of Ni which has much higher density than rGO [41]. The surface area increases as the metal content is increased from 10% to 15% and decreases with further increment of the metal loading of 20%. This trend observed for the surface area is similar to that mentioned in the literature [42–44]. Ni_{15}/rGO shows the highest surface area, possibly because of a better dispersion and smaller particle size of the Ni on rGO. Uniform dispersion of the nickel metal on rGO was achieved with 15% loading, which is indicated from the FESEM/EDX-mapping. It is proposed that the 15% Ni loading led to small Ni particle size formation and lower metal agglomeration. The pore diameter of Ni_{15}/rGO is proven to be the smallest among the different Ni/rGO catalysts, suggesting a high concentration of smaller pores and hence reflecting the highest surface area [45]. A further increase of Ni loading to 20 wt% resulted in a lower surface area of the catalyst. Based on a previous study by Jang et al. [46], this could be attributed to the agglomeration of nickel particles on the rGO.
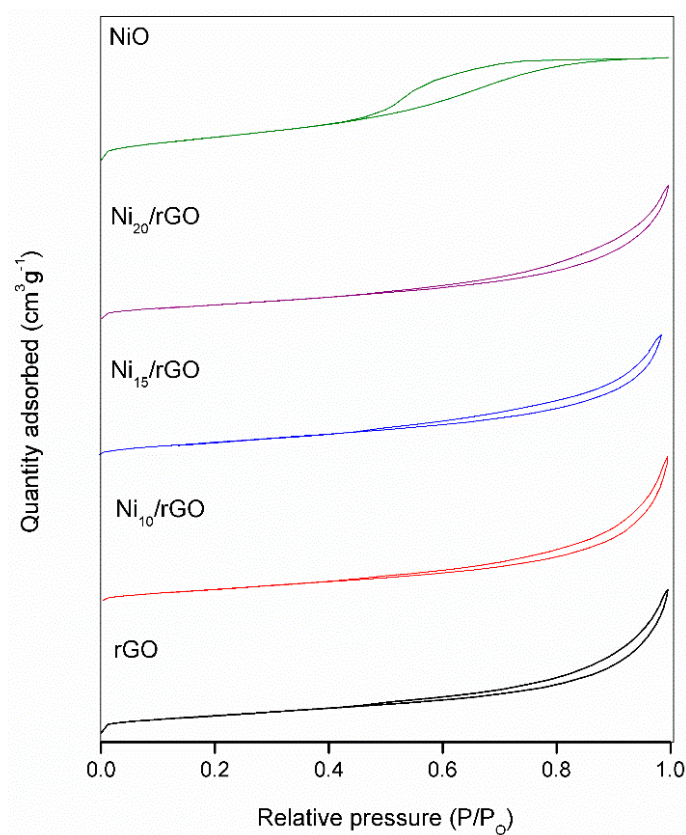

Figure 4. Isotherm of rGO, NiO and Ni/rGO catalysts.

The FTIR spectra of rGO and Ni_{15}/rGO catalyst are presented in Figure 5, while the assignments of each absorption peak are listed in Table 2. A strong broad absorption at 3420 cm^{-1} is attributed to the O-H stretching vibration, very likely coming from oxygen-containing functional groups at the edge of the graphene sheets [47]. The peak at 1725 cm^{-1} reflects the vibration band of carbonyl functional groups (C=O, COOH) and the medium broad peak at 1087 cm^{-1} is assigned to the stretching mode of C-O and C-O-C. The presence of skeletal C=C in rGO is observed from the stretching and bending of C=C at 1574 cm^{-1} and 800 cm^{-1}, respectively. The spectrum of Ni_{15}/rGO shows no formation of new peaks after metal loading, so the FTIR spectrum of Ni/rGO is similar to that of rGO in terms of peak position of each functional group, possibly suggesting that the oxygen functional groups in rGO were not degraded in the synthesis step, in line with the TGA result that indicated a high stability of rGO.
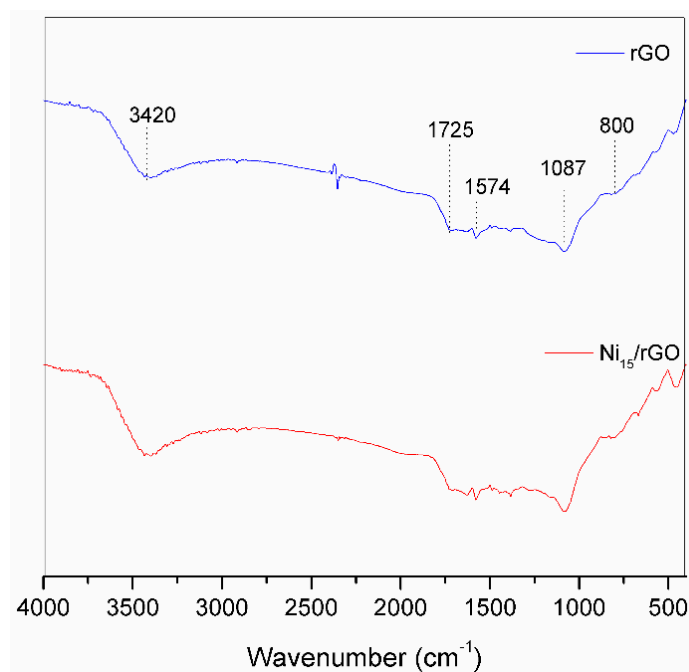

Figure 5. FTIR spectra of rGO and Ni_{15}/rGO catalyst.

Table 2. FTIR peak assignments for Ni/rGO and rGO catalysts.

Absorption Peak (cm^{-1})	Assigned Functional Group
3420	O-H stretching vibration
1725	C=O/COOH vibration
1574	C=C stretching
1087	C-O, C-O-C stretching
800	C=C bending

Temperature programmed reduction (TPR) analysis using H_2 was performed to study the relation between reducibility and metal-support interaction. The TPR profiles of the Ni/rGO catalysts are presented in Figure 6. The profile provided the amount of H_2 gas consumed by the catalysts at different temperatures caused by redox reaction between H_2 and NiO according to the following equation: $NiO_{(s)} + H_{2(g)} \rightarrow Ni^{\circ}_{(s)} + H_2O_{(g)}$ [13]. From Figure 6, the three catalysts show strong signals at temperatures around 400–600 °C caused by the reduction of Ni^{2+} species that strongly interact with the graphene support [48,49]. Ni_{15}/rGO shows the highest reduction temperature owing to the strongest metal-support interaction. This can be explained as due to the fact the energy needed to overcome the interactions of NiO and rGO increases with the increasing strength of such interactions. Furthermore, the strongest interactions in Ni_{15}/rGO also relates to the high dispersion of the NiO on the rGO support which is proven by EDX mapping and highest BET surface area [42]. In addition, a shoulder peak is

observed at around 300–350 °C for all catalysts. This peak is assigned to the surface species of bulk Ni that are weakly contacting with the support, called 'free' nickel species [40,50]. The intensity of this peak increases with increasing Ni loading and it became apparent in Ni_{20}/rGO catalyst possibly because of the agglomeration of larger NiO crystallites on the surface, in agreement with the XRD and BET results. Based on Table 3, H_2 consumption reflects the order of Ni_{10}/rGO < Ni_{15}/rGO < Ni_{20}/rGO which follows the amount of Ni concentrations in the samples. In comparison to some literature values, the reduction temperature of Ni/rGO is relatively lower than those of Ni/Al_2O_3 [12,40,51], Ni/SiO_2 [13] and Ni/ZrO_2 [15], which reflects the higher reducibility of Ni^{2+} in our Ni/rGO catalysts.
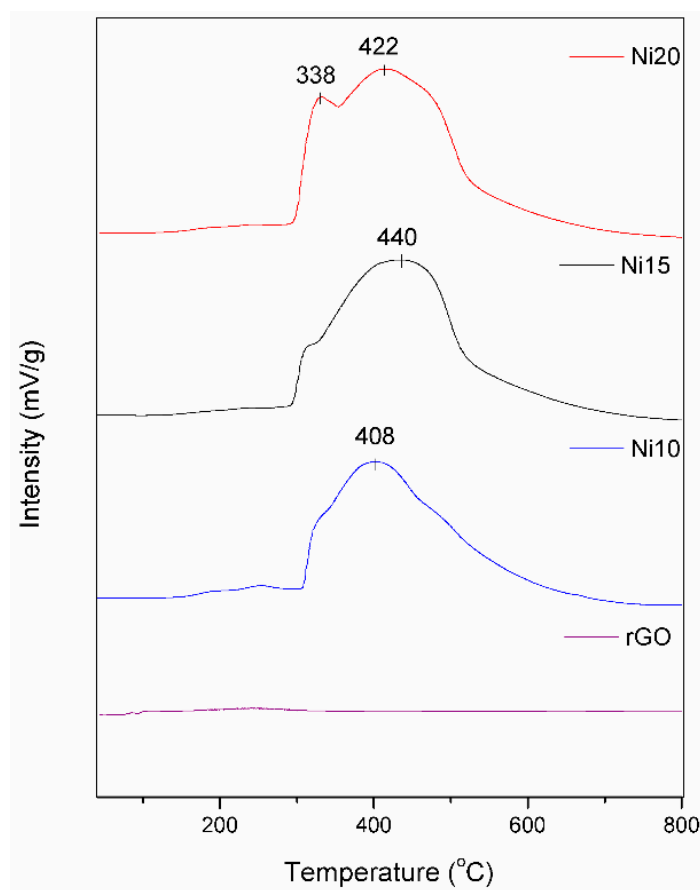

Figure 6. H_2-TPR profile of rGO and Ni/rGO catalysts.

Table 3. Reducibility, basicity and activity data of Ni/rGO catalyst.

Catalyst	CO_2 Desorption Temperature (°C)	H_2 Consumption (mmol/g.cat)	CO_2 Conv. (%)	Methane Selectivity (%)	Methane STY (g/kg(cat)·h)	TOF (s^{-1})
rGO	-	-	0	0	0	0
Ni_{10}/rGO	541	1.75	44.3	99	19.9	9.7×10^{-6}
Ni_{15}/rGO	557	2.20	55.3	100	24.9	9.2×10^{-6}
Ni_{20}/rGO	545	2.36	40.5	100	18.2	6.2×10^{-6}

Figure 7 shows the CO_2-TPD spectra of the Ni/rGO catalysts and rGO support. NiO is also evaluated for control purposes. CO_2-TPD evaluates the CO_2 adsorption and activation capability of the catalyst for methanation. rGO does not show any significant desorption, indicating that it contains only a small number of basic sites. On the other hand, NiO shows a broad signal for the γ peak at 583 °C. When Ni is supported on rGO, a sharp and intense desorption peak at ~550 °C appears. This γ peak corresponds to the strong basic sites [49,52], responsible for chemical adsorption of CO_2 [2]. On closer inspection, there is relatively small peak at around 115 °C for all Ni/rGO catalysts, indicating the weak basic sites. From this result, it is therefore deduced that the basic sites of the catalyst contribute to the

presence of Ni active metal which is basic in nature. The low signal for NiO in the chromatogram is most probably due to the agglomeration of the Ni particles [3]. Once supported, the dispersion of Ni is enhanced, and new interactions based on Lewis acid-base interaction of electron transfer between Ni and support were created which led to higher number of basic sites. The desorption temperature of CO_2 from the catalyst is tabulated in Table 3. As shown in Table 3, the desorption temperature of Ni_{15}/rGO is the highest since it has strongest basic sites and metal-support interaction.
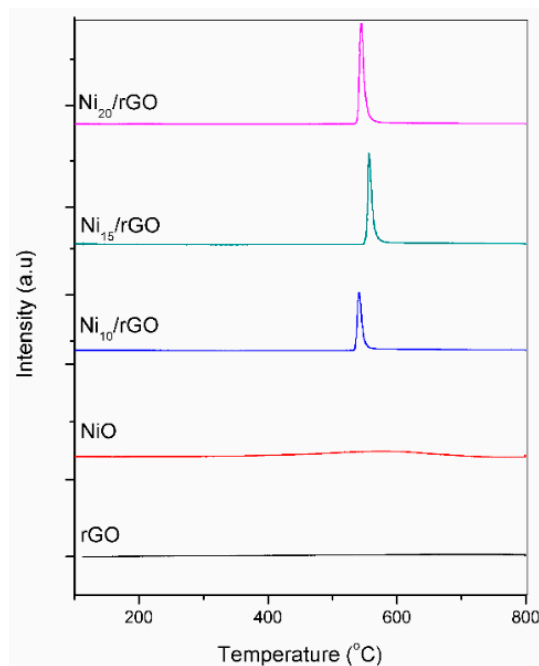

Figure 7. CO_2-TPD profile of rGO, catalysts.

The FESEM-EDX mapping images of Ni/rGO catalysts are displayed in Figure 8. The multilayer nanosheets of graphene can be clearly observed in each FESEM image of the catalysts. From the EDX mapping, it can be observed that the Ni is dispersed well on the surface of graphene. This is due to the high surface area and porous structure of graphene. The higher density of Ni on the graphene is due to higher Ni content loaded on the graphene. As the Ni content increase, there could be agglomeration occurred for Ni_{20}/rGO catalyst as observed in the EDX mapping. Agglomeration is also proven from the lowest surface area and high Ni crystallite size of Ni_{20}/rGO among other Ni/rGO catalysts.
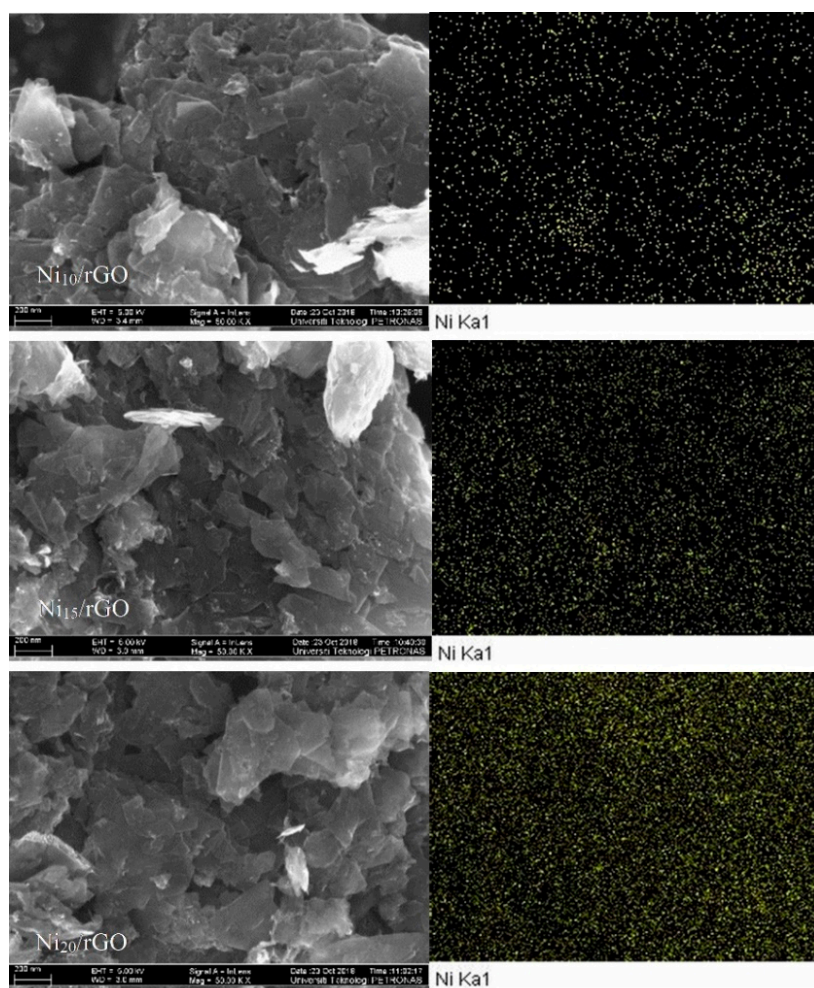
Figure 8. FESEM-images and EDX-mapping of Ni/rGO catalysts.

2.2. Catalytic Activity

The catalytic activity of Ni/rGO catalyst is presented in Table 3, outlining the CO_2 conversion and CH_4 selectivity. For comparison purposes, Raney nickel was also studied for the catalytic conversion of CO_2 into CH_4. NiO has low conversion of CO_2 which is only 5.7%, suggesting the necessity of a catalyst support in the CO_2 methanation. The low conversion of CO_2 on NiO nanoparticles is related to the lower number of basic sites and hydrogen consumption of the catalysts due to agglomeration of the particles. After being supported on rGO, the conversion of CO_2 and product selectivity to methane was notably increased. This is possibly due to the presence of rGO which improve the dispersion of Ni and reduces agglomeration. Consequently, the specific activity per Ni atom increases for CO_2 methanation. The trend for the activities of the catalysts is directly correlated with their respective S_{BET}, where Ni_{15}/rGO shows the highest conversion. The higher the surface area, the higher the conversion because the number of active sites increases due to the presence of more pores. The trend is also related to the basic sites which act as the active sites for reaction and the strength of the metal-support interactions. As shown in the CO_2-TPD and H_2-TPR result, Ni_{15}/rGO has the strongest basic sites due to the high temperature for CO_2 desorption and high reduction temperature. This indicates that CO_2 first dissociates on the basic sites of the catalyst prior to its conversion into methane. Previous studies found that Ni metal became the active site for hydrogen dissociation which was then added to C form methane [53]. A graphical representation of the conversion of CO_2 into methane on the Ni/rGO catalyst from this study is displayed in Figure 9. Overall, both physicochemical and activity profiles of catalysts were significantly affected by the variation of Ni content. Physicochemical investigations suggested

15 wt% of Ni as an optimum amount for the rGO-supported Ni catalyst. Activity data confirmed the Ni$_{15}$/rGO catalyst as the most efficient catalyst in terms of methane productivity (24.9 g/kg·cat·h), followed by Ni$_{10}$/rGO which has high TOF. Ni$_{10}$/rGO has highest TOF as it has the lowest number of basic sites.
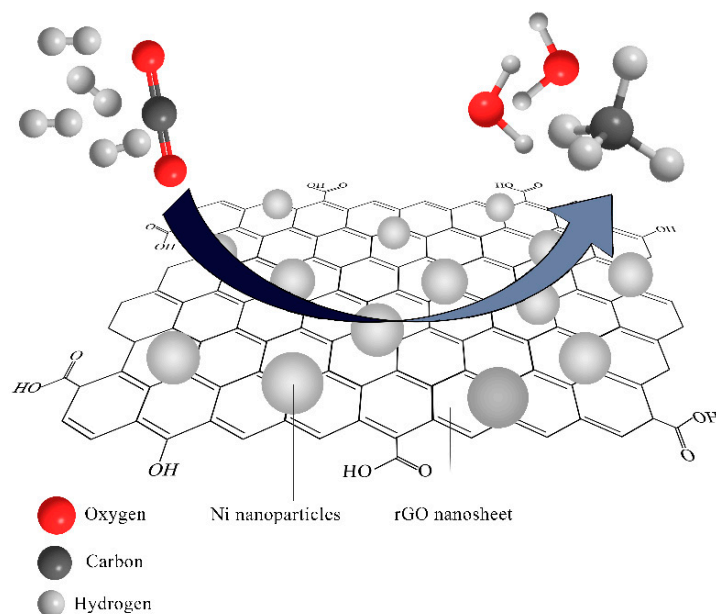

Figure 9. CO_2 conversion to CH_4 on Ni/rGO catalyst.

Apart from that, a comparative study of the current catalyst with the recently reported data [16,41,42,48] for CO_2 hydrogenation methanation is presented in Table 4. As depicted from the tabulated data, the synthesized catalyst showed good activity for methane synthesis and good CO_2 conversion as compared to the catalysts supported on other conventional supports such as Al_2O_3, SiO_2, alumina, MCM-41, SBA-15 and MSU-F. In this work, Ni/rGO exhibited high selectivity which is due to its high CO_2 desorption temperature and CO_2 uptake of the catalysts. The high selectivity is possibly due to the low temperature used in this reaction because the thermodynamic analysis of CO_2 methanation revealed that a lower temperature of reaction suppresses the production of byproducts especially CO [8,54,55].

Table 4. Activity comparison of the synthesized Ni-based catalyst with recent reported data.

Catalyst	T (°C)	P (bar)	Ni Loading (%)	X_{CO2} (%)	S_{CH4} (%)	Ref.
Ni/rGO	240	10	15	55.3	100	This study
Ni/Al$_2$O$_3$	350	1	25	74	99	[42]
Ni/MSN	300	1	5	64.1	99.9	[41]
Ni/ZrO$_2$	300	1	8	71.9	69.5	[48]
Ni/CeO$_2$	340	1	10	91.1	100	[16]

3. Materials and Methods

3.1. Materials

Commercial reduced graphene oxide (rGO) from Sigma Aldrich (St. Louis, MO, USA cat. 796034) was used as received and was characterized thoroughly to understand its properties as outlined in Section 3.3. Nickel nitrate hexahydrate (Ni(NO$_3$)$_2$·6H$_2$O), was obtained from Merck (Darmstadt, Germany). All the solutions were prepared using distilled water.

3.2. Synthesis of Ni-Based Catalyst

NiO catalyst was synthesized based on precipitation method [56] in which 3.96 g (0.012 mol) of $Ni(NO_3)_2 \cdot 6H_2O$ was added to 20 mL distilled water. The solution was constantly stirred with the simultaneous addition of 20 mL of 15% NaOH solution. After 15 min, a green precipitate of $Ni(OH)_2$ was obtained that was separated using vacuum filtration and dried at 100 °C. Finally, the sample was calcined at 400 °C for 2 h, producing NiO black powder.

Ni/rGO catalysts were synthesized via the incipient wetness impregnation method. Initially, 10, 15 and 20 wt.% (relative to the weight of rGO) of Ni precursors were added dropwise to commercial rGO support using an aqueous solution prepared by dissolving required amount of $Ni(NO_3)_2 \cdot 3H_2O$. The volume of impregnating solution was adjusted to the volume of the support. The impregnated sample was left for 12 h. Then, it was dried at 80 °C for 12 h in oven before calcined at temperature 400 °C for 2 h. Each catalyst was characterized as described in Section 3.3.

3.3. Material Characterization

Thermogravimetric analysis (TGA) of rGO support was conducted using a TGA/DSC STARe thermogravimetric analyser (Mettler Toledo, Columbus, OH, USA) equipped with a GC10 gas controller over the temperature range of 25 °C to 900 °C (heating ramp: 20 °C/min) in a N_2 atmosphere. The purpose of TGA was to understand the thermal properties and analyse weight loss profile of rGO support which is used for determination of catalyst calcination temperature.

The Raman spectrum of rGO was obtained using a HR800 spectrometer Horiba Jobin Yvon (Kyoto, Japan) with a 514 nm green laser as excitation source in the Raman shift of 400 to 4000 cm^{-1} range to identify the structure and degree of disorder in carbon-based material of the rGO support.

X-ray diffractograms for rGO and Ni/rGO catalysts were recorded on a powder diffractometer (X'Pert[3] Powder & Empyrean, PANalytical, Malver, UK) with Cu Kα radiation source between 2θ of 5° to 90° (scanning step of 0.01°/step) on continuous scanning. Interlayer spacing (*d*), crystal stack height (L_c), crystallite size (L_a) and estimated number of layers (N_{GP}) were obtained from Equations (2) to (5) respectively:

$$\lambda = 2d \sin\theta \tag{2}$$

$$L_c = K\lambda/B \cos\theta \tag{3}$$

$$L_a = K_2\lambda/B \cos\theta \tag{4}$$

$$N_{GP} = L_c/d \tag{5}$$

where λ is wavelength of Cu Kα radiation (1.5418 Å), *K* is shape factor (0.89), K_2 is Warren Form Factor (1.84) and *B* is line broadening at half maximum of peak.

Surface area and porosity (SAP) analysis of rGO, and Ni/rGO catalysts were performed using an ASAP 2020 analyser (Micromeritics, Norcross, GA, USA) with N_2 as adsorbate. The surface area was determined from the BET model, pore size and volume were determined using the BJH method and micropore analysis was carried out using t-plot analysis.

A Fourier-transform infrared (FTIR) spectrophotometer (Spectrum One, Perkin Elmer, Waltham, MA, USA) was used to study the functional groups of the rGO support and Ni_{15}/rGO catalyst in the range of 400–4000 cm^{-1} with a resolution of 4 cm^{-1}. Sample pellets were prepared by grinding with KBr.

Hydrogen temperature-programmed reduction (H_2-TPR) of the catalysts was carried out using a TPD/R/O 110 MS (Thermo scientific, Waltham, MA, USA) equipped with a thermal conductivity detector (TCD) to evaluate the reducibility and metal-support interaction of the catalysts. The analysis was performed in temperature range of 30 °C to 800 °C at heating rate of 10 °C/min in the gas flow of 5 vol.% H_2/N_2 ratio with flow rate of 20 mL/min.

CO_2 temperature-programmed desorption (CO_2-TPD) of rGO, Ni/rGO and NiO was carried out on a TPD/R/O (1100CE) instrument equipped with TCD. The sample was pretreated at 100 °C under

helium flow (20 mL/min) and cooled down to 75 °C. Sorption study was carried out using CO_2 gas (10 mL/min) for 30 min. Then, temperature was decreased to 40 °C. Then, desorption was performed using He (20 mL/min) in the temperature range of 40–800 °C at a heating rate of 10 °C/min.

The surface morphologies of Ni/rGO catalysts were observed by field emission scanning electron microscopy equipped with energy dispersive X-ray spectroscopy (FESEM-EDX). The analysis was performed using a Supra55 Variable Pressure (VP) system (Zeiss, Jena, Germany) under 5 kV accelerating voltage, magnification range of 5 to 100 k× and 4 nm working distance.

3.4. Catalytic Activity of Ni/rGO

The scheme of the methanation setup is presented in Figure 10. Each catalyst was reduced beforehand using H_2-temperature programmed reduction (H_2-TPR) under 5% H_2 in argon at the total rate of 20 mL/min from temperature 50 to 500 °C with a heating ramp of 10 °C/min. CO_2 methanation was performed for 2 h in a 100 mL autoclave slurry reactor (Parr 4593 with a regular Parr 4848, Parr, Moline, IL, USA) at 10 bar with 240 °C reaction temperature and 500 rpm agitator speed. Feed gas was supplied to the reactor in 1:4 molar ratio of CO_2:H_2. Catalyst (0.5 g) was placed in 40 mL dodecane liquid phase to form a 1.25% (*w/v*) slurry of catalyst in solvent. A natural gas analyzer (Perkin Elmer Clarus 580 GC) was used for the analysis of reagents and product using ASTMD 1945 standard method. The reaction condition was chosen based on previous literature [22,57] that used slurry reactor with some modification at lower temperature. CO_2 conversion, CH_4 selectivity, space time yield (STY) and turnover frequency (TOF) are calculated from the respective equations below:

$$X_{CO_2}(\%) = \frac{n_{CO_2,in} - n_{CO_2,out}}{n_{CO_2,in}} \times 100\% \tag{6}$$

$$S_{CH_4}(\%) = \frac{n_{CH_4,out}}{\sum n_{product_{out}}} \times 100\% \tag{7}$$

$$STY = \frac{\text{Quantity of methane (g)}}{\text{Weight of catalyst (kg.cat)} \times \text{time (h)}} \tag{8}$$

$$TOF = \frac{\text{Mole of } CO_2 \text{ consumed}}{\text{Number of basic sites (mmol·g cat)} \times \text{mass of catalyst (g)} \times \text{time (s)}} \tag{9}$$

A: Feed Gas (H_2/CO_2)
B: Liquid Sampling Valve
C: Stirrer
D: Reaction Cell
E: Heater
F: Gas Sampling Valve
G: Temperature Sensor
H: Pressure Gauge
I: Reactor Controller
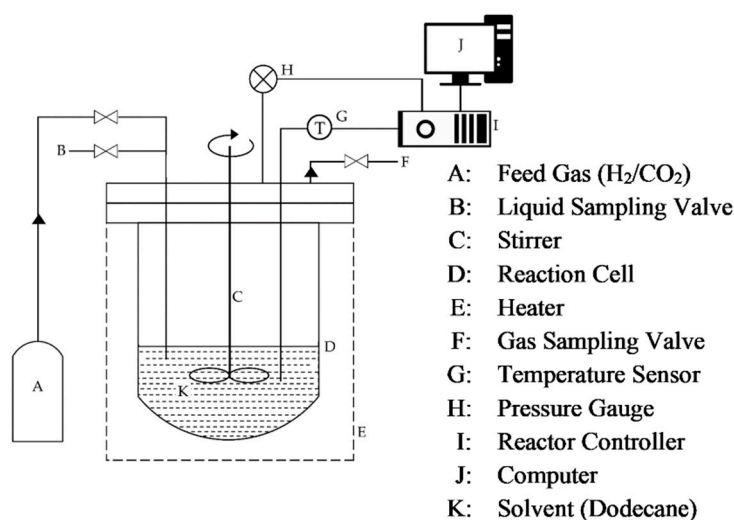J: Computer
K: Solvent (Dodecane)

Figure 10. Schematic diagram of three-phase slurry reactor.

Initial experiments were repeated two times to check for reproducibility. Gas chromatograph analysis are, in general, reproducible within a maximum of 6% but mostly within a few percent.

4. Conclusions

Ni/rGO catalysts with three different Ni loadings were successfully synthesized via the incipient wetness impregnation method and their catalytic activity towards CO_2 methanation was assessed. It was found that the variation of Ni loading affected both the physicochemical properties and catalytic activity. A Ni loading of 15 wt% relative to the weight of rGO has the highest surface area and strongest basic sites. Due to these properties, Ni_{15}/rGO shows highest conversion of CO_2. The high surface area of the catalysts provide active sites for the chemical reaction whereas strong basic sites of catalysts serve as sites for CO_2 dissociation.

Author Contributions: M.S.S. and N.D.M.R. designed the experiment; N.D.M.R. and K.M.L. performed and collect data; M.S.S. supervised and administrated the work; N.D.M.R. wrote the original draft preparation; M.S.S., I.U.D. and P.P. revise, review and edit the paper. All authors have read and agreed to the published version of the manuscript.

Conflicts of Interest: The authors declare no conflict of interest.

References

1. Din, I.U.; Shaharun, M.S.; Naeem, A.; Tasleem, S.; Ahmad, P. Revalorization of CO_2 for methanol production via ZnO promoted carbon nanofibers based Cu-ZrO_2 catalytic hydrogenation. *J. Energy Chem.* **2019**, *39*, 68–76. [CrossRef]

2. Wang, X.; Zhu, L.; Liu, Y.; Wang, S. CO_2 methanation on the catalyst of Ni/MCM-41 promoted with CeO_2. *Sci. Total Environ.* **2018**, *625*, 686–695. [CrossRef] [PubMed]

3. Le, T.A.; Kim, T.W.; Lee, S.H.; Park, E.D. Effects of Na content in Na/Ni/SiO_2 and Na/Ni/CeO_2 catalysts for CO and CO_2 methanation. *Catal. Today* **2018**, *303*, 159–167. [CrossRef]

4. Sabatier, P.; Senderens, J.B. Direct hydrogenation of oxides of carbon in presence of various finely divided metals. *CR Acad. Sci.* **1902**, *134*, 689–691.

5. Bligaard, T.; Nørskov, J.K.; Dahl, S.; Matthiesen, J.; Christensen, C.H.; Sehested, J. The Brønsted–Evans–Polanyi relation and the volcano curve in heterogeneous catalysis. *J. Catal.* **2004**, *224*, 206–217. [CrossRef]

6. Garbarino, G.; Bellotti, D.; Riani, P.; Magistri, L.; Busca, G. Methanation of carbon dioxide on Ru/Al_2O_3 and Ni/Al_2O_3 catalysts at atmospheric pressure: Catalysts activation, behaviour and stability. *Int. J. Hydrog. Energy* **2015**, *40*, 9171–9182. [CrossRef]

7. Kuznecova, I.; Gusca, J. Property based ranking of CO and CO_2 methanation catalysts. *Energy Procedia* **2017**, *128*, 255–260. [CrossRef]

8. Su, X.; Xu, J.; Liang, B.; Duan, H.; Hou, B.; Huang, Y. Catalytic carbon dioxide hydrogenation to methane: A review of recent studies. *J. Energy Chem.* **2016**, *25*, 553–565. [CrossRef]

9. Meshkani, F.; Rezaei, M. Nanocrystalline MgO supported nickel-based bimetallic catalysts for carbon dioxide reforming of methane. *Int. J. Hydrog. Energy* **2010**, *35*, 10295–10301. [CrossRef]

10. Xu, L.; Lian, X.; Chen, M.; Cui, Y.; Wang, F.; Li, W.; Huang, B. CO_2 methanation over Co Ni bimetal-doped ordered mesoporous Al_2O_3 catalysts with enhanced low-temperature activities. *Int. J. Hydrog. Energy* **2018**, *43*, 17172–17184. [CrossRef]

11. Hwang, S.; Lee, J.; Hong, U.G.; Jung, J.C.; Koh, D.J.; Lim, H.; Byun, C.; Song, I.K. Hydrogenation of carbon monoxide to methane over mesoporous nickel-M-alumina (M=Fe, Ni, Co, Ce, and La) xerogel catalysts. *J. Ind. Eng. Chem.* **2012**, *18*, 243–248. [CrossRef]

12. Mihet, M.; Lazar, M.D. Methanation of CO_2 on Ni/γ-Al_2O_3: Influence of Pt, Pd or Rh promotion. *Catal. Today* **2018**, *306*, 294–299. [CrossRef]

13. Gac, W.; Zawadzki, W.; Słowik, G.; Sienkiewicz, A.; Kierys, A. Nickel catalysts supported on silica microspheres for CO_2 methanation. *Microporous Mesoporous Mater.* **2018**, *272*, 79–91. [CrossRef]

14. Takano, H.; Kirihata, Y.; Izumiya, K.; Kumagai, N.; Habazaki, H.; Hashimoto, K. Highly active Ni/Y-doped ZrO_2 catalysts for CO_2 methanation. *Appl. Surf. Sci.* **2016**, *388*, 653–663. [CrossRef]

15. Hu, L.; Urakawa, A. Continuous CO_2 capture and reduction in one process: CO_2 methanation over unpromoted and promoted Ni/ZrO_2. *J. CO2 Util.* **2018**, *25*, 323–329. [CrossRef]

16. Zhou, G.; Liu, H.; Cui, K.; Jia, A.; Hu, G.; Jiao, Z.; Liu, Y.; Zhang, X. Role of surface Ni and Ce species of Ni/CeO_2 catalyst in CO_2 methanation. *Appl. Surf. Sci.* **2016**, *383*, 248–252. [CrossRef]

17. Cai, M.; Wen, J.; Chu, W.; Cheng, X.; Li, Z. Methanation of carbon dioxide on Ni/ZrO_2-Al_2O_3 catalysts: Effects of ZrO_2 promoter and preparation method of novel ZrO_2-Al_2O_3 carrier. *J. Nat. Gas Chem.* **2011**, *20*, 318–324. [CrossRef]

18. Novoselov, K.S.; Geim, A.K.; Morozov, S.V.; Jiang, D.; Zhang, Y.; Dubonos, S.V.; Grigorieva, I.V.; Firsov, A.A. Electric field effect in atomically thin carbon films. *Science* **2004**, *306*, 666–669. [CrossRef]

19. Marcano, D.C.; Kosynkin, D.V.; Berlin, J.M.; Sinitskii, A.; Sun, Z.; Slesarev, A.; Alemany, L.B.; Lu, W.; Tour, J.M. Improved synthesis of graphene oxide. *ACS Nano* **2010**, *4*, 4806–4814. [CrossRef]

20. Park, S.; An, J.; Potts, J.R.; Velamakanni, A.; Murali, S.; Ruoff, R.S. Hydrazine-reduction of graphite-and graphene oxide. *Carbon* **2011**, *49*, 3019–3023. [CrossRef]

21. Julkapli, N.M.; Bagheri, S. Graphene supported heterogeneous catalysts: An overview. *Int. J. Hydrog. Energy* **2015**, *40*, 948–979. [CrossRef]

22. Lefebvre, J.; Götz, M.; Bajohr, S.; Reimert, R.; Kolb, T. Improvement of three-phase methanation reactor performance for steady-state and transient operation. *Fuel Process. Technol.* **2015**, *132*, 83–90. [CrossRef]

23. Behkish, A.; Men, Z.; Inga, J.R.; Morsi, B.I. Mass transfer characteristics in a large-scale slurry bubble column reactor with organic liquid mixtures. *J. Chem. Eng. Sci.* **2002**, *57*, 3307–3324. [CrossRef]

24. Din, I.U.; Shaharun, M.S.; Naeem, A.; Tasleem, S.; Johan, M.R. Carbon nanofibers based copper/zirconia catalysts for carbon dioxide hydrogenation to methanol: Effect of copper concentration. *Chem. Eng. J.* **2018**, *334*, 619–629. [CrossRef]

25. Shen, J.; Yan, B.; Shi, M.; Ma, H.; Li, N.; Ye, M. One step hydrothermal synthesis of TiO_2-reduced graphene oxide sheets. *J. Mater. Chem.* **2011**, *21*, 3415–3421. [CrossRef]

26. Deerattrakul, V.; Dittanet, P.; Sawangphruk, M.; Kongkachuichay, P. CO_2 hydrogenation to methanol using Cu-Zn catalyst supported on reduced graphene oxide nanosheets. *J. CO2 Util.* **2016**, *16*, 104–113. [CrossRef]

27. Malard, L.; Pimenta, M.; Dresselhaus, G.; Dresselhaus, M. Raman spectroscopy in graphene. *Phys. Rep.* **2009**, *473*, 51–87. [CrossRef]

28. Guerrero-Contreras, J.; Caballero-Briones, F. Graphene oxide powders with different oxidation degree, prepared by synthesis variations of the Hummers method. *Mater. Chem. Phys.* **2015**, *153*, 209–220. [CrossRef]

29. Gogotsi, Y.; Presser, V. *Carbon Nanomaterials*, 2nd ed.; CRC Press: Boca Raton, FL, USA, 2014.

30. Hidayah, N.; Liu, W.-W.; Lai, C.-W.; Noriman, N.; Khe, C.-S.; Hashim, U.; Lee, H.C. Comparison on graphite, graphene oxide and reduced graphene oxide: Synthesis and characterization. *AIP Conf. Proc.* **2017**, *1892*, 150002.

31. Lavin-Lopez, M.P.; Paton-Carrero, A.; Sanchez-Silva, L.; Valverde, J.L.; Romero, A. Influence of the reduction strategy in the synthesis of reduced graphene oxide. *Adv. Powder Technol.* **2017**, *28*, 3195–3203. [CrossRef]

32. Cançado, L.; Takai, K.; Enoki, T.; Endo, M.; Kim, Y.; Mizusaki, H.; Jorio, A.; Coelho, L.; Magalhaes-Paniago, R.; Pimenta, M. General equation for the determination of the crystallite size L a of nanographite by Raman spectroscopy. *Appl. Phys. Lett.* **2006**, *88*, 163106. [CrossRef]

33. Dervishi, E.; Ji, Z.; Htoon, H.; Sykora, M.; Doorn, S.K. Raman spectroscopy of bottom-up synthesized graphene quantum dots: Size and structure dependence. *Nanoscale* **2019**, *11*, 16571–16581. [CrossRef] [PubMed]

34. Ma, H.; Ma, K.; Ji, J.; Tang, S.; Liu, C.; Jiang, W.; Yue, H.; Liang, B. Graphene intercalated Ni-SiO_2/GO-Ni-foamcCatalyst with enhanced reactivity and heat-transfer for CO_2 methanation. *Chem. Eng. Sci.* **2018**, *194*, 10–21. [CrossRef]

35. Callister, W.D.; Rethwisch, D.G. *Materials Science and Engineering*, 9th ed.; Wiley: Pasig, Philippines, 2014.

36. Li, Y.; Yu, Y.; Wang, J.-G.; Song, J.; Li, Q.; Dong, M.; Liu, C.-J. CO oxidation over graphene supported palladium catalyst. *Appl. Catal. B Environ.* **2012**, *125*, 189–196. [CrossRef]

37. Hu, D.; Gao, J.; Ping, Y.; Jia, L.; Gunawan, P.; Zhong, Z.; Xu, G.; Gu, F.; Su, F. Enhanced Investigation of CO Methanation over Ni/Al_2O_3 Catalysts for Synthetic Natural Gas Production. *Ind. Eng. Chem. Res.* **2012**, *51*, 4875–4886. [CrossRef]

38. Lowell, S.; Shields, J.E.; Thomas, M.A.; Thommes, M. *Characterization of Porous Solids and Powders: Surface Area, Pore Size and Density*; Springer Science & Business Media: Berlin, Germany, 2012; Volume 16.

39. Ramimoghadam, D.; Hussein, M.Z.B.; Taufiq-Yap, Y.H. Hydrothermal synthesis of zinc oxide nanoparticles using rice as soft biotemplate. *Chem. Cent. J.* **2013**, *7*, 136. [CrossRef] [PubMed]

40. Moghaddam, S.V.; Rezaei, M.; Meshkani, F.; Daroughegi, R. Synthesis of nanocrystalline mesoporous Ni/Al$_2$O$_3$SiO$_2$ catalysts for CO$_2$ methanation reaction. *Int. J. Hydrog. Energy* **2018**, *43*, 19038–19046. [CrossRef]

41. Aziz, M.; Jalil, A.; Triwahyono, S.; Mukti, R.; Taufiq-Yap, Y.; Sazegar, M. Highly active Ni-promoted mesostructured silica nanoparticles for CO$_2$ methanation. *Appl. Catal. B Environ.* **2014**, *147*, 359–368. [CrossRef]

42. Daroughegi, R.; Meshkani, F.; Rezaei, M. Enhanced activity of CO$_2$ methanation over mesoporous nanocrystalline Ni–Al$_2$O$_3$ catalysts prepared by ultrasound-assisted co-precipitation method. *Int. J. Hydrog. Energy* **2017**, *42*, 15115–15125. [CrossRef]

43. Zhang, Z.; Tian, Y.; Zhang, L.; Hu, S.; Xiang, J.; Wang, Y.; Xu, L.; Liu, Q.; Zhang, S.; Hu, X. Impacts of nickel loading on properties, catalytic behaviors of Ni/γ–Al$_2$O$_3$ catalysts and the reaction intermediates formed in methanation of CO$_2$. *Int. J. Hydrog. Energy* **2019**, *44*, 9291–9306. [CrossRef]

44. Wierzbicki, D.; Baran, R.; Dębek, R.; Motak, M.; Grzybek, T.; Gálvez, M.E.; Da Costa, P. The influence of nickel content on the performance of hydrotalcite-derived catalysts in CO$_2$ methanation reaction. *Int. J. Hydrog. Energy* **2017**, *42*, 23548–23555. [CrossRef]

45. Zhang, L.; Bian, L.; Zhu, Z.; Li, Z. La-promoted Ni/Mg-Al catalysts with highly enhanced low-temperature CO$_2$ methanation performance. *Int. J. Hydrog. Energy* **2018**, *43*, 2197–2206. [CrossRef]

46. Jang, M.S.; Phan, T.N.; Chung, I.S.; Lee, I.-G.; Park, Y.-K.; Ko, C.H. Metallic nickel supported on mesoporous silica as catalyst for hydrodeoxygenation: Effect of pore size and structure. *J. Res. Chem. Intermediat.* **2018**, *44*, 3723–3735. [CrossRef]

47. Ren, Y.; Wang, J.; Huang, X.; Ding, J. The synthesis of polypyrrole@ Mn$_3$O$_4$/reduced graphene oxide anode with improved coulombic efficiency. *Electrochim. Acta* **2015**, *186*, 345–352. [CrossRef]

48. Jia, X.; Zhang, X.; Rui, N.; Hu, X.; Liu, C.-J. Structural effect of Ni/ZrO$_2$ catalyst on CO$_2$ methanation with enhanced activity. *Appl. Catal. B Environ.* **2019**, *244*, 159–169. [CrossRef]

49. Romero-Sáez, M.; Dongil, A.B.; Benito, N.; Espinoza-González, R.; Escalona, N.; Gracia, F. CO$_2$ methanation over nickel-ZrO$_2$ catalyst supported on carbon nanotubes: A comparison between two impregnation strategies. *Appl. Catal. B Environ.* **2018**, *237*, 817–825. [CrossRef]

50. Vita, A.; Italiano, C.; Pino, L.; Frontera, P.; Ferraro, M.; Antonucci, V. Activity and stability of powder and monolith-coated Ni/GDC catalysts for CO$_2$ methanation. *Appl. Catal. B Environ.* **2018**, *226*, 384–395. [CrossRef]

51. Lin, J.; Ma, C.; Wang, Q.; Xu, Y.; Ma, G.; Wang, J.; Wang, H.; Dong, C.; Zhang, C.; Ding, M. Enhanced low-temperature performance of CO$_2$ methanation over mesoporous Ni/Al$_2$O$_3$-ZrO$_2$ catalysts. *Appl. Catal. B Environ.* **2019**, *243*, 262–272. [CrossRef]

52. Liang, C.; Wei, T.; Wang, H.; Yu, Z.; Dong, D.; Zhang, S.; Liu, Q.; Hu, G.; Hu, X. Impacts of La Addition on Formation of the Reaction Intermediates over Alumina and Silica Supported Nickel Catalysts in Methanation of CO$_2$. *J. Energy Inst.* **2019**, *93*, 723–738. [CrossRef]

53. Aldana, P.A.U.; Ocampo, F.; Kobl, K.; Louis, B.; Thibault-Starzyk, F.; Daturi, M.; Bazin, P.; Thomas, S.; Roger, A.C. Catalytic CO$_2$ valorization into CH$_4$ on Ni-based ceria-zirconia. Reaction mechanism by operando IR spectroscopy. *Catal. Today* **2013**, *215*, 201–207. [CrossRef]

54. Sahebdelfar, S.; Takht Ravanchi, M. Carbon dioxide utilization for methane production: A thermodynamic analysis. *J. Petroleum Sci. Eng.* **2015**, *134*, 14–22. [CrossRef]

55. Rönsch, S.; Schneider, J.; Matthischke, S.; Schlüter, M.; Götz, M.; Lefebvre, J.; Prabhakaran, P.; Bajohr, S. Review on methanation—From fundamentals to current projects. *Fuel* **2016**, *166*, 276–296. [CrossRef]

56. Jeevanandam, P.; Pulimi, V. Synthesis of nanocrystalline NiO by sol-gel and homogeneous precipitation methods. *Indian J. Chem.* **2012**, *51A*, 586–590.

57. Lefebvre, J.; Bajohr, S.; Kolb, T. A comparison of two-phase and three-phase CO$_2$ methanation reaction kinetics. *Fuel* **2019**, *239*, 896–904. [CrossRef]